# SPHERICAL HARMONIC ANALYSIS OF STEADY PHOTOSPHERIC FLOWS, II

DAVID H. HATHAWAY

*Space Science Laboratory, NASA Marshall Space Flight Center, Huntsville, AL 35812, U.S.A.*

(Received 29 January, 1991; in revised form 5 July, 1991)

**Abstract.** The use of the spherical harmonic functions to analyse the nearly steady flows in the solar photosphere is extended to situations in which $B_0$, the latitude at disk center, is nonzero and spurious velocities are present. The procedures for extracting the rotation profile and meridional circulation are altered to account for the seasonal tilt of the Sun's rotation axis toward and away from the observer. A more robust and accurate method for separating the limb shift and meridional circulation signals is described. The analysis procedures include the ability to mask out areas containing spurious velocities (velocity-like signals that do not represent true flow velocities in the photosphere). The procedures are shown to work well in extracting the various flow components from realistic artificial data with a broad, continuous spectrum for the supergranulation. The presence of this supergranulation signal introduces errors of a few $m\,s^{-1}$ in the measurements of the rotation profile, meridional circulation, and limb shift from a single Doppler image. While averaging the results of 24 hourly measurements has little effect in reducing these errors, an average of 27 daily measurements reduces the errors to well under $1\,m\,s^{-1}$.

## 1. Introduction

In a previous paper (Hathaway, 1987; hereafter referred to as Paper I), an analysis technique was described for extracting the various components of the flows observed in the solar photosphere. Orthogonal polynomials were used to characterize the flow components with the spherical hermonics being used for the nearly steady, horizontal flows. A similar approach has also been suggested by Snodgrass (1984).

In presenting the analysis technique in Paper I, several simplifying assumptions were made and the testing was done with rather unrealistic artificial data. The Sun's rotation axis was assumed to be in the plane of the sky so that the equator passed through disk center. The rotation axis was also assumed to be aligned with one axis of the imaging array. Although it was recognized that spurious velocities are often seen near active regions, no mechanism was offered for dealing with these signals. The artificial data used in Paper I to test the analysis technique contained reasonable rotation, limb shift, and meridional circulation signals, but the motions used to represent the supergranules and giant cells were highly simplified (the full spectrum for these convective flows contained only 15 spectral components).

In the present paper, more useful and robust analysis procedures are presented and tested with realistic synthetic data. The data that are to be analyzed by these procedures are assumed to be full-disk, line-of-sight velocity measurements such as those obtained with the various imaging instruments for helioseismology. Each velocity image should be obtained over a time interval that is less than half the period of the 5 min oscillations. The individual images must then be averaged in time to remove the 5 min oscillations

*Solar Physics* **137:** 15–32, 1992.

while not introducing substantial smearing due to solar rotation. A weighted average over about 20 min, as described by Hathaway (1988a), can reduce the signal due to the $p$-mode oscillations to nearly 1 m s$^{-1}$ while keeping the errors due to the rotational translation of the superganule pattern to a similar level for images with about 256 by 256 pixels.

Many of the constraints imposed on the data in Paper I will be relaxed in this paper. The seasonal tilt of the Sun's rotation axis toward and away from the observer is explicitly accounted for in what follows. The position angle of the Sun's rotation axis with respect to the imaging array may take on any value and the image may be flattened into an elliptical shape by the effects of atmospheric refraction or rectangular pixels on the detector. In addition, portions of the visible disk may be masked out to exclude areas such as active regions and the data to be analyzed may not extend to the extreme limb of the Sun.

## 2. Artificial Data

Artificial data have been produced for testing the analysis procedures. The photospheric Doppler velocities are simulated using the process described by Hathaway (1988b). The horizontal flows in the photosphere are represented by the spherical harmonic functions $Y_l^m(\theta, \phi)$, where $\theta$ is the colatitude measured from the north pole and $\phi$ is the longitude which increases toward the west limb. The vector components of any horizontal flow can be given by the poloidal, $S_l^m$, and toroidal, $T_l^m$, spectral coefficients with

$$U_\theta(\theta, \phi) = \sum_{l=0}^{l_{\max}} \sum_{m=-l}^{+l} \left[ S_l^m \frac{\partial Y_l^m}{\partial \theta} + T_l^m \frac{1}{\sin\theta} \frac{\partial Y_l^m}{\partial \phi} \right] \tag{1}$$

and

$$U_\phi(\theta, \phi) = \sum_{l=0}^{l_{\max}} \sum_{m=-l}^{+l} \left[ S_l^m \frac{1}{\sin\theta} \frac{\partial Y_l^m}{\partial \phi} - T_l^m \frac{\partial Y_l^m}{\partial \theta} \right], \tag{2}$$

where $U_\theta$ is the meridional velocity, $U_\phi$ is the longitudinal velocity, and $l_{\max}$ is the largest spherical harmonic degree to be included in the representation.

The axisymmetric flows, differential rotation and meridional circulation, are represented in this manner by modes with spherical harmonic order $m$ of zero. Upon differentiating these spherical harmonic functions the meridional circulation is given by

$$U_\theta^0(\theta) = -\sum_{l=1}^{l_{\max}} S_l^0 [l(l+1)]^{1/2} \overline{P}_l^1(\cos\theta) \tag{3}$$

and the rotation and differential rotation are given by

$$U_\phi^0(\theta) = \sum_{l=1}^{l_{\max}} T_l^0 [l(l+1)]^{1/2} \overline{P}_l^1(\cos\theta), \tag{4}$$

where $\overline{P}_l^1(\cos\theta)$ is an associated Legendre polynomial of degree $l$ and order 1. The

associated Legendre polynomials used here are normalized so that

$$\int_{-1}^{1} [\bar{P}_l^m(\cos\theta)]^2 \, \mathrm{d}\cos\theta = 1 \, . \tag{5}$$

The artificial data used for testing the analysis procedures include a rotation profile like that given by Scherrer, Wilcox, and Svalgaard (1980). It is represented in terms of the spectral coefficients by

$$T_1^0 = 1593 \text{ m s}^{-1} \, , \tag{6}$$

$$T_3^0 = -33 \text{ m s}^{-1} \, , \tag{7}$$

and

$$T_5^0 = -3 \text{ m s}^{-1} \, . \tag{8}$$

The data also include a meridional circulation which is directed toward the poles with peak flow velocities of about 20 m s$^{-1}$ in the low latitudes. This meridional circulation is represented in terms of the spectral coefficients by

$$S_2^0 = 8 \text{ m s}^{-1} \tag{9}$$

and

$$S_4^0 = -2 \text{ m s}^{-1} \, . \tag{10}$$

The nonaxisymmetric modes represent the convective motions – primarily the supergranulation for $l < 500$. A broad spectrum with a peak amplitude at $l \sim 100$ is used for these motions with

$$S_l^m = 85 [e^{-l/90}(1 - e^{-l^3/80^3})]^{1/2} [l(l+1)(2l+1)]^{-1/2} e^{-i\Phi} \text{ m s}^{-1} \tag{11}$$

and

$$T_l^m = 0.1 \, S_l^m \, , \tag{12}$$

where $\Phi$ is a random phase for each mode. This gives a kinetic energy spectrum which closely approximates the results of the analysis on Doppler data from Mt. Wilson Observatory (Hathaway *et al.*, 1989) for $l > 50$.

The horizontal velocity field derived from the full spectrum is projected onto the line-of-sight using

$$V(\theta, \phi) = U_\theta(\theta, \phi)[\sin B_0 \sin\theta - \cos B_0 \cos\theta \cos\phi] + \\ + U_\phi(\theta, \phi)[\cos B_0 \sin\phi] \, , \tag{13}$$

where $B_0$ is the latitude at disk center and $\phi$ is the longitude measured from the central meridian toward the west limb. A convention adopted throughout this paper is that flows away from the observer (redshifts) are positive.

The convective limb shift is not well represented by the spherical harmonic functions

since it is a function of the angular distance from disk center and is thus not easily mapped to heliographic latitudes and longitudes. (The limb shift is mostly due to the correlation of bright granule centers with upflows and dark intergranule lanes with downflows. This gives a net upflow when averaged over a pixel.) For the artificial data, a limb shift function like that given by Cavallini, Ceppatelli, and Righini (1986) for Fe I $\lambda$5576 is used and is represented by a line-of-sight velocity

$$V_{\mathrm{LS}}(\rho) = \sum_{n=0}^{n_{\max}} C_n (1 - \cos\rho)^n , \tag{14}$$

where $\rho$ is the heliocentric angle from disk center. The coefficients used in the artificial data are

$$C_0 = -540 \text{ m s}^{-1} , \tag{15}$$

$$C_1 = 140 \text{ m s}^{-1} , \tag{16}$$

$$C_2 = 140 \text{ m s}^{-1} , \tag{17}$$

and

$$C_3 = 260 \text{ m s}^{-1} . \tag{18}$$

This gives a blue shift (negative line-of-sight velocity) of 540 m s$^{-1}$ at disk center that approaches zero near the limb.

The artificial data also include a gravitational redshift of 632 m s$^{-1}$ and the velocity signal associated with the motion of an observer at Mt. Wilson Observatory on July 4, 1988 at 17:30 UT. The solar parameters are also taken from those corresponding to this time with a semi-diameter $S_0$ = 945.37 arcsec and latitude at disk center $B_0$ = 3.23°.

Several versions of the artificial data were generated for testing purposes. Most of these were projected onto arrays of 256 by 256 pixels in which the solar image had a diameter of 222 pixels and the spectrum extended to $l_{\max}$ = 256. Some images were projected onto arrays of 512 by 512 pixels in which the solar diameter was 444 pixels. For these larger images the convection spectrum extended to $l_{\max}$ = 512.

## 3. The Analysis Procedures

The analysis procedures described in this section consist of several steps which are to be executed in the prescribed order to extract the various flow components. The first step (described in Section 3.1) involves determining image parameters such as size, shape, and position and constructing a data mask to eliminate regions with spurious velocities. In the second step (described in Section 3.2) the gravitational redshift and the velocity signal due to the motion of the observer are removed from the data. The third step (Section 3.3) involves a preliminary determination of the convective limb shift and its removal from the data. In the fourth step (Section 3.4) the data are mapped from the image on to a regular grid in heliospheric coordinates. The rotation profile is

determined and removed from the data in the fifth step (Section 3.5) and the meridional circulation is measured and subtracted from the data in the sixth step (Section 3.6). In the seventh step (Section 3.7) the results of the preliminary limb shift determination from step 3 are corrected for the presence of the meridional circulation discovered in step 6. In the final step (Section 3.8) the spectrum of the nonaxisymmetric convective motions is determined.

### 3.1. Image measurements and data mask

Before the analysis can begin several measurements concerning the data must be made. The image scale, in arcsec or radians per pixel, must be determined along with the position of the center of the image and its shape. These measurements can be obtained from an intensity image associated with the velocity data. The limb of the Sun is located by finding the locus of points with a local maximum in the radial gradient of the intensity. These points are then used to determine the ellipse that minimizes the rms error between the measured radius and the predicted radius for that ellipse. This process requires a multidimensional routine such as AMOEBA described by Press *et al.* (1986) to determine the coordinates of the center, the lengths of the semi-major and semi-minor axes, and the position angle of the semi-minor axis of the ellipse that best fits the limb position data.

In most cases there will be areas on the disk containing data that are suspected of having spurious velocities due to the presence of active regions or due to scattered light. A data mask can be constructed which multiplies the velocity data with zeros in the unwanted areas and ones in the desirable areas. The use of this mask introduces some added work in the analysis procedures but is often required by the nature of the data.

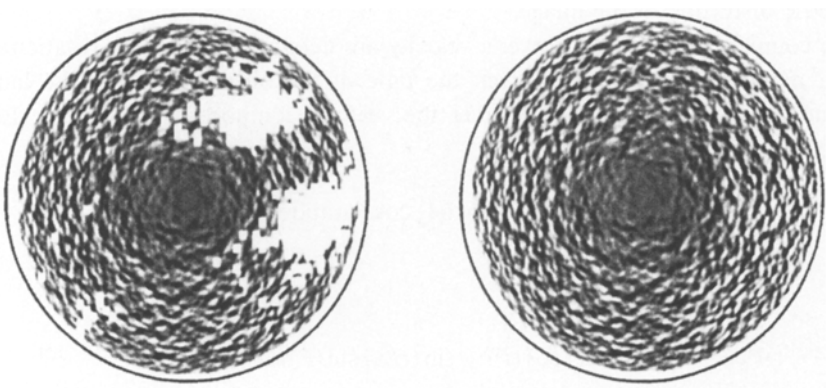


Fig. 1. Artificial data with masked regions shown on the left and masked regions filled on the right. The rotation, limb shift, and observer motion velocity signals have been removed from these images to better reveal the supergranulation. The position of the solar limb is indicated by the circle surrounding each image.

In the results presented here, data whthin 5% of the limb are omitted and a data mask which covers the active regions seen on the Sun on July 4, 1988 is used.

An image of the masked artificial data is shown on the left-hand side of Figure 1 with the rotation, limb shift, and observer motion signals removed so that the weaker flows are more evident. These data are used in this section to illustrate and test the performance of the analysis procedures. One aspect of the analysis procedure requires filling in the masked areas with proxy data consisting of an estimate of the velocity due to the rotation, meridional circulation, and limb shift along with data from other parts of the disk to represent the supergranulation. The result of filling in the masked areas in this manner is shown on the right-hand side of Figure 1.

### 3.2. Velocity corrections

The next step in processing the velocity image is to remove both the gravitational redshift (taken to be 632 m $s^{-1}$) and the velocity field due to the motion of the observer. If the three components of the observer's velocity with respect to the center of the Sun are given as a radial velocity, $V_R$, away from disk center, a velocity, $V_X$, parallel to the solar equator and toward the east limb, and a velocity, $V_Y$, parallel to the Sun's rotation axis and toward the Sun's south pole, then the corrected velocity is given by

$$V(p_1, \Theta) = V(p_1, \Theta) - 632 - V_R(1 - \tfrac{1}{2}\rho_1^2) + \\ + V_X \rho_1 \sin\Theta - V_Y \rho_1 \cos\Theta \quad \text{m s}^{-1}, \tag{19}$$

where $\rho_1$ is the angular distance from disk center in radians and $\Theta$ is the position angle measured counterclockwise from the north pole position. The measurements of the coordinate positions must, of course, account for the position of the center of the image, the position angle of the Sun's rotation axis with respect to the imaging array, and any geometric distortion of the image.

The components of the observer's velocity are determined from the rotational and orbital motions of the Earth. Given the time of the observation and the latitude, longitude, and altitude of the observer the velocity components due to the Earth's rotation are given by

$$V_\Omega = [2000\pi(6378 + h)/86164] \cos(\text{latitude}) \quad \text{m s}^{-1}, \tag{20}$$

$$V_R = V_\Omega \sin(HA) \cos(\delta), \tag{21}$$

$$V_X = V_\Omega \cos(HA) \cos(P) - \sin(HA) \sin(P) \sin(\delta)], \tag{22}$$

and

$$V_Y = V_\Omega [\cos(HA) \sin(P) + \sin(HA) \cos(P) \sin(\delta)], \tag{23}$$

where $h$ is the altitude in km, $HA$ is the hour angle of the Sun, $\delta$ is the declination angle of the Sun, and $P$ is the position angle of the Sun's rotation axis. The velocity com-

ponents due to the Earth's orbital motion are given by

$$V_O = \frac{2\pi(1.49598 \times 10^{11})}{(365.256 \times 86400)}(1 - e^2)^{-1/2} \quad \mathrm{m\,s^{-1}}, \tag{24}$$

$$V_R = V_O e \sin(\lambda - \lambda_0), \tag{25}$$

$$V_\lambda = V_O[1 + e\cos(\lambda - \lambda_0)], \tag{26}$$

$$V_X = -V_\lambda \cos[7.15^\circ \cos(\lambda - \lambda_\odot)], \tag{27}$$

and

$$V_Y = -V_\lambda \cos[7.15^\circ \sin(\lambda - \lambda_\odot)], \tag{28}$$

where $e = 0.01671$ is the eccentricity of the Earth's orbit, $\lambda$ is the ecliptic longitude corresponding to the time of the observation, $\lambda_0 \approx 282.9^\circ$ is the longitude of the perihelion passage, and $\lambda_\odot \approx 75.9^\circ$ is the longitude at which the Earth passes northward across the Sun's equatorial plane.

### 3.3 Preliminary limb shift determination

An accurate determination of the limb shift requires three steps. In this preliminary step the line-of-sight velocity is averaged over the position angle $\Theta$ in a series of radial bins. Since this average contains the average of the meridional circulation signal, the meridional circulation must then be determined in a later step. The results of the preliminary determination are then corrected for the presence of the meridional circulation.

This preliminary step requires a mapping from the angular distance, $\rho_1$, from disk center to $\rho$, the heliocentric value of this angle, according to the formula

$$\sin(\rho + \rho_1) = \frac{\rho_1}{S_0}, \tag{29}$$

where $S_0$, the semi-diameter of the solar image, should be measured in radians as well. The data are then averaged over position angle $\Theta$ according to

$$V_{\mathrm{LS}}(\rho) = \frac{1}{2\pi}\int_0^{2\pi} [V(\rho, \Theta)M(\rho, \Theta) + V_{\mathrm{FILL}}(\rho, \Theta)[1 - M(\rho, \Theta)]]\,\mathrm{d}\Theta, \tag{30}$$

where $M$ is the data mask and

$$V_{\mathrm{FILL}}(\rho, \Theta) = V_{\mathrm{ROT}}(\rho, \Theta) + V_{\mathrm{MC}}(\rho, \Theta) + V_{\mathrm{LS}}(\rho) \tag{31}$$

is used to fill in the masked areas with $V_{\mathrm{ROT}}$, $V_{\mathrm{MC}}$, and $V_{\mathrm{LS}}$ which represent canonical or best estimates of the rotation, meridional circulation, and limb shift signals. The difficulty with the mask in this step is that the average given by the first term in (30) can easily be influenced by masking out sections of the rotation signal. Without the mask

the rotation signal gives no contribution to the average since it is antisymmetric about the central meridian. The second term in (30) introduces a correction to the average by filling in the masked areas with appropriate data. This technique for filling in the masked areas will be employed in later steps as well.

In practice, the integral in (30) is implemented by summing the data in a number of bins of finite width in $\rho$. Since the average value of $\rho$ is weighted toward the outside half of the bin by the larger number of points in that region, corrections to $V_{\mathrm{LS}}$ are included to reposition the measurements on the desired positions in $\rho$. The results are then fit to a polynomial of the form given by (14) with $n_{\max} \sim 4$ to give the limb shift coefficients $C_n$. Larger values of $n_{\max}$ tend to introduce oscillations in the polynomial fit and smaller values may not capture the functional form of the limb shift.

This polynomial fit to the data is then removed from the data itself. Note again that the average given by (30) includes the average of the meridional circulation signal so that part of the meridional circulation signal is also removed from the data at this point. This process will be accounted for in determining the meridional circulation in a later step.

### 3.4. Map to heliographic coordinates

Once the limb shift signal is removed from the data the remaining velocity signal and the data mask are mapped to a heliographic coordinate grid, $(\theta, \phi)$, using

$$\sin\theta\cos\phi = \cos B_0 \cos\rho - \sin B_0 \sin\rho \cos\Theta\,, \tag{32}$$

$$\sin\theta\sin\phi = -\sin\rho\sin\Theta\,, \tag{33}$$

and

$$\cos\theta = \sin B_0 \cos\rho + \cos B_0 \sin\rho \cos\Theta\,. \tag{34}$$

The heliographic grid has equally spaced points in both longitude and $\cos\theta$. (Although the zeros of the associated Legendre polynomials have nearly equal spacing in colatitude, the data is acquired with nearly equal spacing in $\cos\theta$. This gives poor sampling intervals at high latitudes and subsequent mixing between the spherical harmonics with high $l$ and low $m$. Since the loss of resolution at high latitudes is unimproved by any subsequent mapping, this situation cannot be improved by mapping onto a grid with equal spacing in $\theta$ even though the high l low $m$ spherical harmonies are well resolved on such a grid.)

The mapping is done by choosing a point on the heliographic grid, finding its position on the original image or mask, and then interpolating using a bi-quadratic fit to the data using the closest point and its four nearest neighbors. Since data within 5% of the limb are masked out, the useful velocity signal is limited to latitudes equatorward of about 70° for the analysis that follows.

### 3.5. Rotation profile determination

The velocity of the solar rotation is obtained from the mapped data with

$$U_\phi^0(\theta)\cos B_0 = \frac{1}{N(\theta)} \int_{\phi_1}^{\phi_2} [V(\theta, \phi)M(\theta, \phi) + \\ + V_{\text{FILL}}(\theta, \phi)[1 - M(\theta, \phi)]]\, W_1(\theta, \phi)\sin\phi\, \mathrm{d}\phi\,, \tag{35}$$

where $\phi_1$ and $\phi_2$ represent the limiting longitudes over which the data are available,

$$N(\theta) = \int_{\phi_1}^{\phi_2} W_1(\theta, \phi)\sin^2\phi\, \mathrm{d}\phi \tag{36}$$

is a normalization factor,

$$V_{\text{FILL}}(\theta, \phi) = V_{\text{ROT}}(\theta, \phi) + V_{\text{MC}}(\theta, \phi) \tag{37}$$

is used to fill in the masked areas with appropriate data, and

$$W_1(\theta, \phi) = \cos^2\phi \tag{38}$$

is a weighting function. Although the use of this weighting function can slightly degrade the performance of this procedure on ideal data, it is useful when dealing with real data

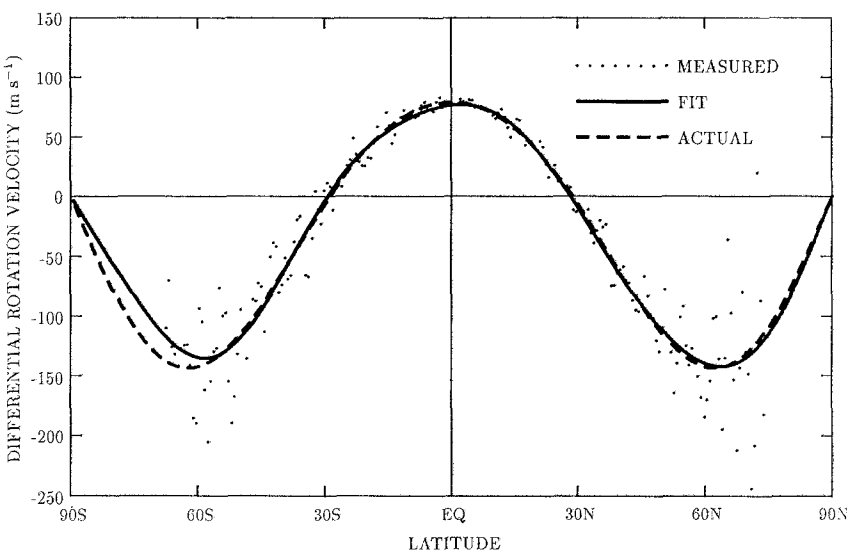


Fig. 2. Differential rotation measurement results. The individual measurements are represented by the dots. The Legendre polynomial fit to the measurements is represented by the solid line. The actual differential rotation that was embedded in the data in included as the dashed line for comparison. Equatorward of 60° the polynomial fit deviates from the actual profile by less than about 3 m s$^{-1}$. These deviations and the scatter in the individual measurements are both due to the supergranulation signal.

which may be unreliable near the limb and thus are given less weight than data near disk center. $V_{\mathrm{ROT}}$ and $V_{\mathrm{MC}}$ in (37) represent canonical or best estimates of the rotation and meridional circulation signals for filling in the masked areas. The functional form for $V_{\mathrm{MC}}$ accounts for the part removed in the preliminary limb shift procedure even though this may represent a very small correction of the results of (35).

The values of $U_\phi^0(\theta)$ obtained from (35) are used to obtain a fit to the associated Legendre polynomials as represented by (4). This fit, with $l_{\max} \sim 8$, is then projected onto the line of sight and substracted from the data. Both the raw rotation profile, $U_\phi^0(\theta)$, and the spectral coefficients, $T_l^0$, are retained as measures of the rotation profile.

The results of this analysis on the artificial data are presented in Figure 2. The dots represent the measurements of the differential rotation velocity at each latitude position while the solid line represents the polynomial fit to these measurements. The dashed line in Figure 2 represents the actual differential rotation profile given by the input spectrum in (6)–(8). The scatter in the individual measurements is due to the presence of the supergranulation signal. While the individual measurements deviate from the actual values by tens of m s$^{-1}$, the polynomial fit is accurate to within about 3 m s$^{-1}$ except at high latitudes were there are little data and only a few supergranules are crossed while evaluating (35). More accurate measures of the rotation profile will require averaging the results from several images to obtain a better statistical sample of the supergranulation. This is discussed in more detail in Section 4.

### 3.6. Meridional circulation determination

In order to make an accurate determination of the meridional circulation careful attention must be paid to the preliminary limb shift analysis. In removing the preliminary limb shift signal, the average of the meridional circulation signal over position angle $\Theta$ was also removed. So, using (3), (13), and (30), we find that the line-of-sight velocity due to the meridional circulation signal is given by

$$\begin{aligned} V_{\mathrm{MC}}(\theta, \phi) = & -\sum_{l=1}^{l_{\max}} S_l^0 [l(l+1)]^{1/2} \{\bar{P}_l^1(\cos\theta) \times \\ & \times [\sin B_0 \sin\theta - \cos B_0 \cos\theta \cos\phi] - \\ & - \frac{1}{2\pi} \int_0^{2\pi} \bar{P}_l^1(\cos\theta) [\sin B_0 \sin\theta - \cos B_0 \cos\theta \cos\phi] \, \mathrm{d}\Theta \} , \end{aligned} \tag{39}$$

where the integral is over the position angle on the solar disk. With some effort the result of this integration can be shown to give

$$\begin{aligned} \frac{1}{2\pi} \int_0^{2\pi} & \bar{P}_l^1(\cos\theta) [\sin B_0 \sin\theta - \cos B_0 \cos\theta \cos\phi] \, \mathrm{d}\Theta = \\ & = \left[\frac{2}{2l+1}\right]^{1/2} \bar{P}_l^0(\sin B_0) \sin\rho \bar{P}_l^1(\cos\rho) . \end{aligned} \tag{40}$$

Thus, the meridional circulation signal at this stage is given by

$$V_{\mathrm{MC}}(\theta, \phi) = -\sum_{l=1}^{l_{\max}} S_l^0 [l(l+1)]^{1/2} F_{\mathrm{MC}}(B_0, \theta, \phi), \tag{41}$$

where

$$F_{\mathrm{MC}}(B_0, \theta, \phi) = \bar{P}_l^1(\cos\theta)[\sin B_0 \sin\theta - \cos B_0 \cos\theta \cos\phi] - \\ - \left[\frac{2}{2l+1}\right]^{1/2} \bar{P}_l^0(\sin B_0) \sin\rho(\theta, \phi) \bar{P}_l^1(\cos\rho(\theta, \phi)). \tag{42}$$

(Note that $\sin\rho \bar{P}_l^1(\cos\rho)$ is a polynomial in $\cos\rho$ just like the limb shift is in (14).) In order to determine the meridional circulation signal, the two-dimensional functional form (41) is used in a fit to the data for $l_{\max} \sim 8$ to obtain the spectral coefficients $S_l^0$. Here again the data mask is used to exclude some regions of the disk and the masked areas are filled in with data that include a canonical meridional circulation signal of the same form as in (41). (This is also the form of the meridional circulation signal used in (37).)

Once the spectral coefficients are determined the meridional circulation signal is reconstructed and removed from the data.

The results of this analysis on the artificial data are shown in Figure 3. The solid line represents the results of the analysis for the meridional circulation. The dashed line

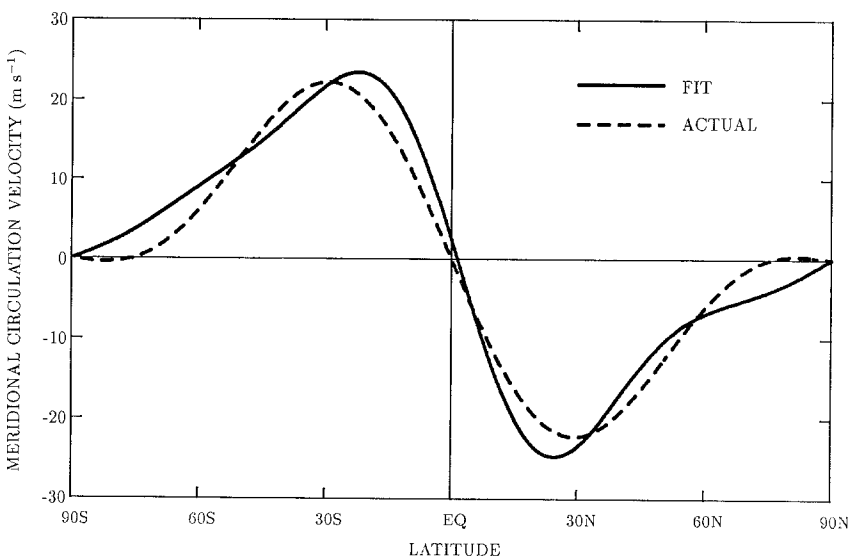


Fig. 3. Meridional circulation results. The functional fit to the meridional circulation is plotted by the solid line as a function of latitude. The actual meridional circulation profile that was embedded in the data is represented by the dashed line. The functional fit agrees with the actual profile to within about 3 m s$^{-1}$. This deviation is due to the presence of the supergranulation signal.

represents the actual input profile. Differences of about 3 m s$^{-1}$ are evident in the results. As it was with the differential rotation signal, these differences are due to the presence of the supergranulation signal and can be further reduced by averaging the results from several different images.

### 3.7 Final limb shift correction

The results of the preliminary limb shift determination can be corrected for the presence of the meridional circulation after the meridional circulation has been calculated. Both the limb signal and its polynomial fit must be corrected with

$$V_{LS}(\rho) = V_{LS}(\rho) + \sum_{l=1}^{l_{max}} S_l^0 [l(l+1)]^{1/2} \left[\frac{2}{2l+1}\right]^{1/2} \times$$

$$\times \bar{P}_l^0(\sin B_0) \sin\rho \bar{P}_l^1(\cos\rho) \tag{43}$$

and the coefficients for the limb shift signal are then given by

$$C_n = C_n + \delta C_n , \tag{44}$$

where $\delta C_n$ is calculated from the correction term in (43).

The final results for the limb shift determination with the artificial data are shown in Figure 4. The dots represent the measurements at individual radial positions while the solid curve represents the results of the polynomial fit. (Note that the measurements stop

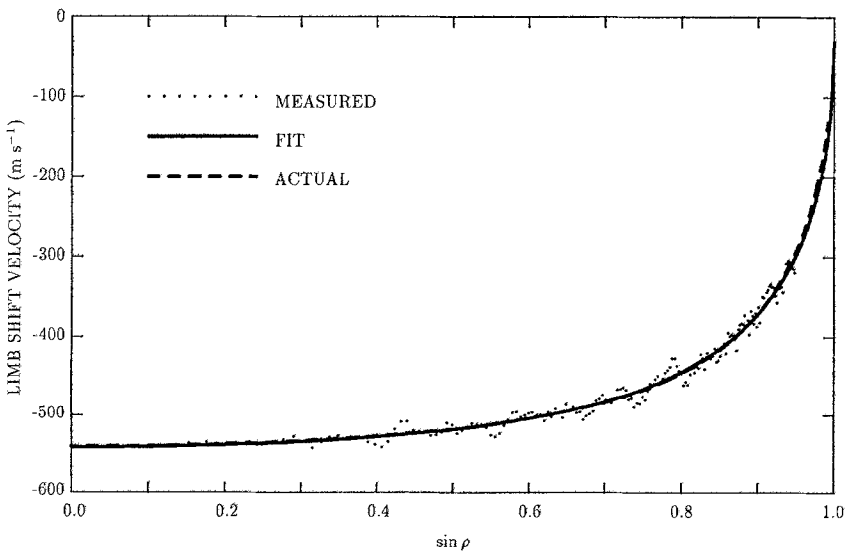


Fig. 4. Final limb shift measurement results. The individual measurements are shown by the dots as a function of distance, sin$\rho$, from disk center. The polynomial fit to the data is represented by the solid line and the actual limb shift profile is represented by the dashed line. The polynomial fit agrees with the actual values to within a few m s$^{-1}$ except for sin$\rho > 0.95$ where the data are marked out and the polynomial fit represents an extrapolation.

at $\sin\rho = 0.95$ since the extreme limb was masked out.) The dashed curve represents the actual limb shift profile embedded in the artificial data. Here again, the errors in the measurements are attributed to the presence of the supergranulation signal.

### 3.8. Convection spectrum determination

After the limb shift, the rotation profile, and the meridional circulation are removed from the data, the remaining data are projected onto the spherical harmonics using

$$A_l^m = \frac{1}{N_l^m} \int_{-1}^{1} \int_{\phi_1}^{\phi_2} [V(\theta, \phi) M(\theta, \phi) + \\ + V_{\text{FILL}}(\theta, \phi)[1 - M(\theta, \phi)]] W_2(\theta, \phi) Y_l^m(\theta, \phi) \, \mathrm{d}\phi \, \mathrm{d}(\cos\theta), \quad (45)$$

where

$$N_l^m = \int_{-1}^{1} \int_{\phi_1}^{\phi_2} W_2(\theta, \phi) [Y_l^m(\theta, \phi)]^2 \, \mathrm{d}\phi \, \mathrm{d}(\cos\theta) \quad (46)$$

is a normalization factor,

$$V_{\text{FILL}}(\theta, \phi) = V(\theta, -\phi) M(\theta, -\phi) \quad (47)$$

is used to fill in the masked areas with data reflected through the central meridian, and $W_2(\theta, \phi)$ is a weighting function that apodizes the data near the limiting longitudes $\phi_1$ and $\phi_2$. At this stage of the analysis the edges of the mask should be smoothed so it falls from unity to zero over several pixels. The effectiveness of smoothing the mask edges and filling in with data from other parts of the disk is evident in the right-hand image in Figure 1. While this gap filling technique preserves the overall spectral content of the image, it should be noted that the data pattern in the field regions will appear to translate retrograde when view over a series of images.

Although the individual spectral coefficients $A_l^m$ represent rather complex combinations of the poloidal and toroidal coefficients $T_l^m$ and $S_l^m$, the kinetic energy of the spectral components can still be determined from them. For the kinetic energy at a given wave number $l$, $\text{KE}_l$, we have

$$\text{KE}_l = \tfrac{1}{2}\rho[l(l+1)] \sum_{m=-l}^{l} [[S_l^m]^2 + [T_l^m]^2], \quad (48)$$

where the $\rho$ in (48) represents the mass density of the photospheric gas. Since we only measure the line-of-sight component of the velocity a factor of 2 must be included in the measured kinetic energy spectrum to account for the velocity component transverse to the line of sight. (This assumes that the velocities are isotropic in the horizontal.) Projection effects on the measured component introduce an additional factor of $4/\pi$. In addition, because of foreshortening near the limb, the amplitudes of the high degree modes will be diminished because they are spatially resolved over a limited area in

heliographic coordinates. We find

$$\mathrm{KE}_l = \rho \frac{4}{\pi} N_l^2 \sum_{m=-l}^{l} [A_l^m]^2 , \tag{49}$$

where

$$N_l = \left( \frac{\arcsin[0.95]}{\arccos\left[\dfrac{2l}{\pi N_D}\right]} \right)^2 \tag{50}$$

represents the ratio of the area (in heliographic coordinates) of the available data to the area over which a mode of degree $l$ is resolved. $N_D$ represents the number of pixels in the diameter of the solar image.

Figure 5 shows the results of the analysis for the convection spectrum obtained from the artificial data. The dots represent the measurement results from (49) while the

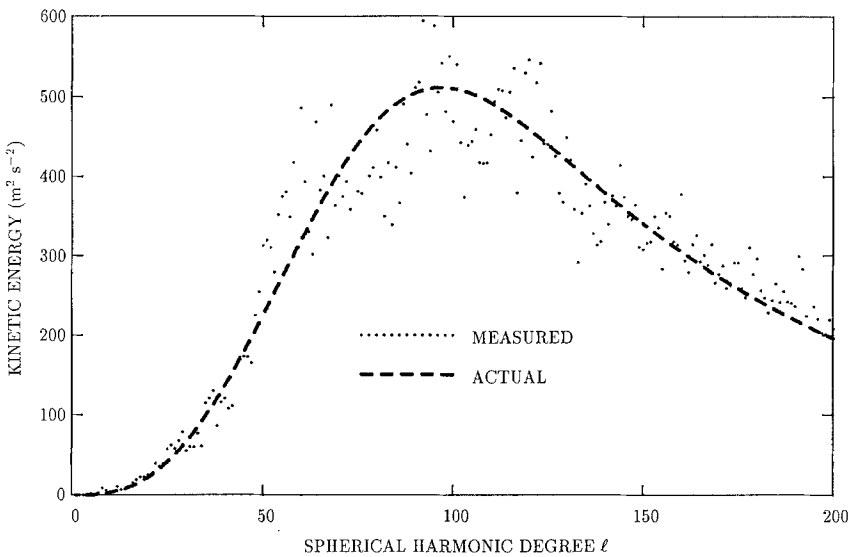


Fig. 5. Kinetic energy spectrum for the convective motions. The dots represent the measured kinetic energy as a function of spherical harmonic degree $l$ as given by (49). The dashed line represents the actual spectrum used in constructing the artificial data.

dashed line represents the input spectrum given by (48). Since there were only 222 pixels across the solar diameter the analysis was limited to $l < 200$. Similar results were obtained with the larger (512 by 512 pixel) images for $l < 400$.

## 4. Long-Term Observations

The analysis techniques presented in the previous section can be used to determine ,the rotation, meridional circulation, and limb shift profiles to within about 3 m $s^{-1}$ from a

single Doppler image. As was noted, this limitation is due to the presence of supergranulation. More accurate measurements will be required for investigating small variations in these profiles such as the torsional oscillations discovered by Howard and LaBonte (1980). This added accuracy can be achieved with long-term observations by averaging the spectral coefficients obtained from images acquired over an extended length of time.

Two time series of artificial data images were generated in an effort to determine the sampling interval and number of images required to reduce the measurement errors. In both time series the supergranulation pattern was made to rotate differentially and evolve in time with a lifetime of about 3 days. For the first time series 24 images were constructed with 1 hour elapsed time between images to represent a single day. For the second time series 27 images were constructed with 1 day elapsed time between images to represent a Carrington rotation of the Sun. Each of these images was analyzed to determine the spectral coefficients that represent the measured flows.

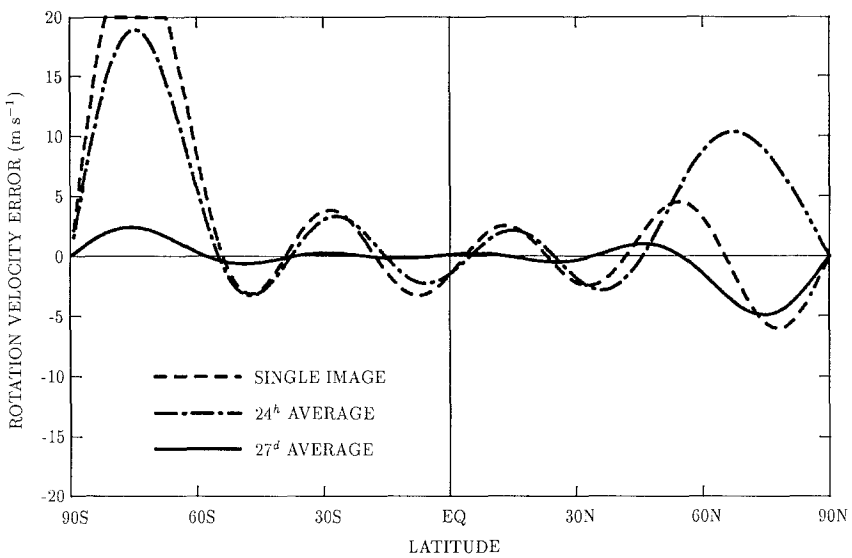


Fig. 6. Rotation velocity measurement errors. The difference between the measured (polynomial fit) rotation profile and the actual rotation profile is plotted as a function of latitude for the results from a single image (dashed line), an average of 24 hourly images (dash-dot line), and an average of 27 daily images (solid line). The average of the 24 hourly measurements shows little improvement over the results from the single image. The average of the 27 daily images gives substantial improvement in the measurements.

Figure 6 illustrates the results of averaging these spectral coefficients to determine the rotation profile. The velocity error is plotted with a deshed line for the results from a single image. The average from the 24 hourly images is plotted with a dash-dot line. The result of this average shows only small differences from the single image result except at the highest latitudes. (Recall that the measurements only extend to about 70° so these high latitude results are extrapolations from the lower latitudes.) The average from the 27 daily images is plotted with a solid line in Figure 6. The result of this average shows

substantial improvement over the single image measurement. The measurement errors are well below 1 m $s^{-1}$ in the lower latitudes. The lack of any substantial improvement in the velocity profile determinations with the average of 24 hourly measurements can be attributed to the lack of substantial changes in the pattern of the supergranulation.

## 5. Conclusions and Discussion

The analysis peocedures presented in Section 3, along with the use of long-term observations as discussed in Section 4, can be used to give an accurate determination of the full spectrum of motions in the solar photosphere. The solar rotation profile, convective limb shift, and meridional circulation can be determined to an accuracy of better than 1 m $s^{-1}$ by averaging the spectral coefficients obtained on a daily basis over a solar rotation. This accuracy should further enhance studies of these flows and their variations over the course of the solar cycle. The analysis procedures also yield an accurate measurement of the spectrum of the supergranulation. A full and accurate determination of these photospheric flows will provide valuable information for our understanding of the dynamics of the solar convention zone and its relation to the solar cycle.

In applying these techniques to solar velocity data, data from every pixel on the disk is used to determine the amplitudes of each spectral component. This has distinct advantages over other techniques that use cuts through the data at various positions to try to separate the different flows. Random errors in the velocity measurement at each pixel made contributions of $\sim N_D^{-1}$ times that error to the measurement of the spectral amplitudes. This was illustrated quite graphically in Paper I for the giant cell spectral component. The largest source of error in these measurements are systematic errors and the mixing between the spectral components caused by poor resolution and spatial coverage. The supergranulation signal was identified as the source of errors in measuring the rotation and meridional circulation profiles shown in Figures 2 and 3. As noted in Section 4, these errors can be reduced by long term averaging to yield measurements accurate to less than 1 m $s^{-1}$.

The method described for determining the rotation profile actually differs little from previous methods (Howard and Harvey, 1970; Scherrer, Wilcox, and Svalgaard, 1980) except for the use of the spherical harmonic functions as the basis for fitting the data. (Snodgrass (1984) has also advocated the use of these functions.) The advantages of using these functions include their orthogonality and the fact that the total angular momentum of the surface layers is given by the lowest order mode. Any variations in the amplitude of this mode indicates a net change in the angular momentum of the photospheric layers.

The method described for extracting the limb shift and the meridional circulation differs substantially from previous methods (Beckers, 1978; Duvall, 1979; LaBonte and Howard, 1982; Snodgrass, 1984; Ulrich *et al.*, 1988). The method described here can cleanly separate the limb shift and meridional circulation signals with an accuracy of about 3 m $s^{-1}$ from a single Doppler image. Averaging the daily spectral coefficients

over a solar rotation reduces the errors to less than 1 m $s^{-1}$. A meridional circulation will redistribute both angular momentum and magnetic fields. Thus, an accurate determination of this flow component is important for our understanding of the solar cycle. Although several previous measurements of the meridional circulation indicate the presence of a poleward flow of 10 to 20 m $s^{-1}$ (Beckers, 1978; Duvall, 1979; LaBonte and Howard, 1982; Snodgrass, 1984; Ulrich *et al.*, 1988), others have found equatorward flows (Pérez Garde *et al.*, 1981) or multicellular and time-dependent circulations (Ribes, Mein, and Mangeney, 1985). Accurate determinations of the structure and temporal evolution of the meridional circulation will no doubt prove to be very interesting.

The use of the spherical harmonic functions to characterize the convective motions (primarily supergranulation) was suggested in Paper I and carried somewhat further here. An accurate determination of the spectrum of these motions is possible when projection effects are accounted for in the analysis. The shape of this spectrum provides important clues concerning the nature of solar and stellar convective flows and their effects on the magnetic fields in these objects.

The analysis procedures described here can accurately determine the nature of the nearly steady photospheric flows. They have been developed and tested to the point that they can now be directly applied to Doppler velocity data. The use of these procedures on data from imaging helioseismology instruments will hopefully reveal many interesting phenomena within the solar photosphere and interior.

## Acknowledgements

Support for this research was provided to Marshall Space Flight Center by the Solar Branch of NASA's Space Physics Division. Additional support was provided by NASA funds and NSF Grant No. PHY89–04035 to the Institute for Theoretical Physics of the University of California, Santa Barbara. The author would like to thank his many colleagues at Marshall Space Flight Center and the Institute for Theoretical Physics for their support and assistance on this research. Suggestions by Ed Rhodes, Roger Ulrich, Tim Brown, Juri Toomre, Gary Glatzmaier, and Jorgen Christensen–Dalsgaard were particularly helpful during the final stages in developing these procedures. Comments by Steve Suess and Tauna Moorehead were helpful in preparing the paper for publication.

## References

Beckers, J. M.: 1978, *Astrophys. J.* **224**, L143.
Cavallini, F., Ceppatelli, G., and Righini, A.: 1986, *Astron. Astrophys.* **163**, 219.
Duvall, T. L., Jr.: 1979, *Solar Phys.* **63**, 3.
Hathaway, D. H.: 1987, *Solar Phys.* **108**, 1.
Hathaway, D. H.: 1988a, *Solar Phys.* **117**, 1.
Hathaway, D. H.: 1988b, *Solar Phys.* **117**, 329.
Hathaway, D. H., Rhodes, E. J., Cacciani, A., and Korzennik, S.: 1989, *Bull. Am. Astron. Soc.* **21**, 829.
Howard, R. and Harvey, J.: 1970, *Solar Phys.* **12**, 23.

Howard, R. and LaBonte, B. J.: 1980, *Astrophys. J.* **239**, L33.
LaBonte, B. J. and Howard, R.: 1982, *Solar Phys.* **80**, 361.
Pérez Garde, M., Vásquez, M., Schwan, H., and Wöhl, H.: 1981, *Astron. Astrophys.* **93**, 67.
Press, W. H., Flannery, B. P., Tuekolsky, S. A., and Vetterling, W. T.: 1986, *Numerical Recipies: The Art of Scientific Computing*, Cambridge University Press, Cambridge.
Ribes, E., Mein, P., and Mangeney, A.: 1985, *Nature* **318**, 170.
Scherrer, P. H., Wilcox, J. M., and Svalgaard, L.: 1980, *Astrophys. J.* **241**, 811.
Snodgrass, H. B.: 1984, *Solar Phys.* **94**, 13.
Ulrich, R. K., Boyden, J. E., Webster, L., Snodgrass, H. B., Padilla, S. P., Gilman, P., and Shieber, T.: 1988, *Solar Phys.* **117**, 291.